Open Research Online

Herschel Observations of a Potential Core-Forming Clump: Perseus B1-E

S. I. Sadavoy[1,2], J. Di Francesco[2,1], Ph. André[3], S. Pezzuto[4], J.-P. Bernard[5,6], S. Bontemps[3], E. Bressert[7,8], S. Chitsazzadeh[1,2], C. Fallscheer[1,2], M. Hennemann[3], T. Hill[3], P. Martin[9], F. Motte[3], Q. Nguyễn Lương[3], N. Peretto[3], M. Reid[9], N. Schneider[3], L. Testi[7,10], G. J. White[11,12], and C. Wilson[13]

[1] Department of Physics and Astronomy, University of Victoria, PO Box 355, STN CSC, Victoria BC Canada, V8W 3P6 e-mail: `ssadavoy@uvic.ca`
[2] National Research Council Canada, Herzberg Institute of Astrophysics, 5071 West Saanich Road, Victoria BC Canada, V9E 2E7
[3] Laboratoire AIM, CEA/DSM-CNRS-Universit Paris Diderot, IRFU/Service d'Astrophysique, CEA Saclay, 91191 Gif-sur-Yvette, France
[4] Istituto di Fisica dello Spazio Interplanetario - INAF, Via del Fosso del Cavaliere, 100, I-00133 Roma, Italy
[5] CNRS, IRAP, 9 Av. colonel Roche, BP 44346, 31028 Toulouse Cedex 4, France
[6] Université de Toulouse, UPS-OMP, IRAP, 31028 Toulouse Cedex 4, France
[7] ESO, Karl Schwarzschild-Strasse 2, D87548 Garching bei Munchen, Germany
[8] School of Physics, University of Exeter, Stocker Road, Exeter EX4 4QL, UK
[9] Canadian Institute for Theoretical Astrophysics, University of Toronto, Toronto, ON, M5S 3H8, Canada
[10] INAF-Osservatorio Astrofisico di Arcetri, Largo E. Fermi 5, 50125 Firenze, Italy
[11] The Rutherford Appleton Laboratory, Chilton, Didcot OX11 0NL, UK
[12] The Open University, Department of Physics and Astronomy, Milton Keynes MK7 6AA, UK
[13] Department of Physics and Astronomy, McMaster University, Hamilton, ON, L8S 4M1, Canada

ABSTRACT

We present continuum observations of the Perseus B1-E region from the *Herschel* Gould Belt Survey. These *Herschel* data reveal a loose grouping of substructures at $160 - 500$ μm not seen in previous submillimetre observations. We measure temperature and column density from these data and select the nine densest and coolest substructures for follow-up spectral line observations with the Green Bank Telescope. We find that the B1-E clump has a mass of ~ 100 $M_{\odot}$ and appears to be gravitationally bound. Furthermore, of the nine substructures examined here, one substructure (B1-E2) appears to be itself bound. The substructures are typically less than a Jeans length from their nearest neighbour and thus, may interact on a timescale of ~ 1 Myr. We propose that B1-E may be forming a first generation of dense cores, which could provide important constraints on the initial conditions of prestellar core formation. Our results suggest that B1-E may be influenced by a strong, localized magnetic field, but further observations are still required.

1. Introduction

Molecular clouds are highly structured regions of dust and gas. They contain dense, small-scale, star-forming "cores" ($\lesssim 0.1$ pc) that are usually clustered into larger-scale clumps and organized along filaments (Williams et al. 2000; Ward-Thompson et al. 2007; Di Francesco et al. 2007; André et al. 2010). The cause of this hierarchical structure, where the large-scale clouds (~ 10 pc) with moderate densities ($\sim 10^2$ cm^{-3}) produce filaments, clumps, and dense cores at higher densities ($\gtrsim 10^4$ cm^{-3}), is not well understood (Bergin & Tafalla 2007).

Molecular clouds form dense cores when diffuse gas is compressed. Current theories for core formation primarily focus on two ideas: that cores form via (1) turbulent compression of diffuse gas (e.g., Larson 1981; Mac Low & Klessen 2004; Dib et al. 2009), or (2) the motion of neutral material between magnetic field lines or ambipolar diffusion (e.g., Mestel & Spitzer 1956; Mouschovias 1976; Kunz & Mouschovias 2009). Both mechanisms and gravity likely play important roles in star formation, but it is unclear whether one mechanism would dominate in all situations (i.e., clustered or isolated star formation and low-mass or high-mass star formation). Furthermore, theoretical studies also suggest that additional processes, such as radiation feedback (i.e., Krumholz et al. 2010) or large-scale shocks associated with converging flows (i.e., Heitsch et al. 2011), can influence molecular cloud structure and thus, core formation. Additionally, recent *Herschel* studies have shown that filaments are very prominent in star forming regions and likely have an important role in the formation of dense substructures in molecular clouds (e.g., André et al. 2010; Arzoumanian et al. 2011).

Surveys of core populations in molecular clouds indicate that cores are confined to regions of high column density. Johnstone et al. (2004) and Kirk et al. (2006) found a relationship between core occurrence and extinction for the Ophiuchus and Perseus clouds, respectively, suggesting that there is a core formation threshold at $A_V \gtrsim 5$. Similarly, Lada et al. (2009) and André et al. (2010) each compared two clouds with different degrees of star formation activity and each found that the more active cloud was composed of higher column density material (by a factor of ~ 10) than the quiescent cloud. These studies emphasize that cores require a minimum column density (ex-

tinction) of material to condense from the bulk cloud (see also Heiderman et al. 2010).

The precursors to cores are difficult to identify. Dense cores are often influenced by processes such as nearby outflows and radiation feedback from a previous epoch of nearby star formation, and observations of them cannot be used to constrain the dynamic properties of the initial core-forming material (Curtis & Richer 2011). Without knowing the *initial* conditions and processes that cause cores to form from diffuse gas, we cannot accurately model their formation or evolution. Thus, identifying and analyzing a core forming region without earlier episodes of star formation would be exceedingly useful to constrain how molecular clouds form star-forming substructures.

In this paper, we use observations from the *Herschel* Gould Belt Survey to explore a ~ 0.1 deg^2 clump roughly $0.7°$ east of the B1 clump (Bachiller & Cernicharo 1986) within the Perseus molecular cloud. This region, hereafter called B1-E, has high extinction ($A_V > 5$) similar to the core formation threshold. Despite this high extinction, previous submillimetre and infrared continuum observations suggest that B1-E contains neither dense cores nor young stellar objects (e.g., Enoch et al. 2006; Kirk et al. 2006; Jørgensen et al. 2007; Evans et al. 2009). In contrast, our *Herschel* observations show substructure that was not detected by these other far-infrared and submillimetre continuum studies. Furthermore, we use recent Green Bank Telescope (GBT) observations to quantify in part the kinematic motions of the densest substructures seen in the *Herschel* data.

We propose that B1-E is forming a first generation of dense cores in a pristine environment. In Section 2, we describe our *Herschel* and GBT observations. In Section 3 we describe the properties we derive from our data. In Section 4 we discuss the implication of our results and compare our observations to theoretical models. Finally, in Section 5 we summarize the paper.

2. Data

2.1. Herschel *Observations*

The western half of Perseus, including B1-E, was observed by the Photodetector Array Camera and Spectrometer (PACS; Poglitsch et al. 2010) and the Spectral and Photometric Imaging Receiver (SPIRE; Griffin et al. 2010) as part of the *Herschel* Gould Belt Survey (André & Saraceno 2005; André et al. 2010). The *Herschel* observations were taken in "parallel mode", resulting in simultaneous coverage at 5 wavelength bands, with the 70 μm and 160 μm PACS channels and the 250 μm, 350 μm, and 500 μm SPIRE channels, over roughly 6 square degrees. The 70 μm observations of B1-E, however, are less sensitive due to the fast scan rate (60″/s) and low emission from cold material (see Section 3.1). Thus, we will not include the 70 μm observations in our discussion. For a full explanation of the observations, see Pezzuto et al. (2012, in preparation).

The PACS and SPIRE raw data were reduced using HIPE version 5.0 and reduction scripts written by M. Sauvage (PACS) and P. Panuzzo (SPIRE) that were modified from the standard pipeline. For SPIRE reduction, we used updated calibration information (version 4). The final maps were created using the *scanamorphos* routine developed by Roussel (2011, submitted to A&A). For consistency with other published maps, we set the pixel scale[1] to the default size from the HIPE mapmaking tools, which results in pixels of sizes 6.4″, 6.0″, 10.0″, and 14.0″ for 160 μm, 250 μm, 350 μm, and 500 μm, respectively. We

also adopt beam sizes of 13.4″, 18.1″, 25.2″, and 36.6″ for the 160 μm, 250 μm, 350 μm, and 500 μm bands respectively[2] (see Griffin et al. 2010; Poglitsch et al. 2010). Assuming a distance to Perseus of 235 pc (Hirota et al. 2008), *Herschel* can detect structure on scales of ~ 0.04 pc at 500 μm. Figure 1 shows a three-colour image of Western Perseus with labels for B1-E and other prominent subregions.

Unlike previous ground-based submillimetre instruments, *Herschel* can detect large-scale diffuse emission (e.g., Schneider et al. 2010; Miville-Deschênes et al. 2010; Arzoumanian et al. 2011). Additionally, *Herschel* has excellent sensitivity to low-level flux. For example, Figure 2 compares SCUBA 850 μm observations of B1-E (smoothed to 23″ resolution; Di Francesco et al. 2008) with the new SPIRE 250 μm observations (at 18″ resolution). The SPIRE 250 μm data show prominent substructures not identified in the SCUBA 850 μm data, though several faint features at 850 μm appear to agree with the brighter structures in the 250 μm map. With the higher sensitivity of *Herschel*, we are able to identify clearly structures in B1-E that were too faint, i.e., $< 3\,\sigma$, to be robust detections with SCUBA.

2.2. GBT Observations

We selected the nine highest peaks in our *Herschel*-derived H$_2$ column density map of B1-E (see Section 3.2) for complementary follow-up observations with the new K-band Focal Plane Array (KFPA) receiver on the GBT[3]. Our targets, hereafter named B1-E1 to B1-E9 according to decreasing peak column density, were observed on 03 March 2011 with single-pointings. We used the KFPA receiver with one beam and four spectral windows to observe each target simultaneously in NH$_3$ (1,1), NH$_3$ (2,2), CCS ($2_1 - 1_0$), and HC$_5$N (9-8) line emission at 23.6945 GHz, 23.7226 GHz, 22.3440 GHz, and 23.9639 GHz, respectively. Similar to Rosolowsky et al. (2008), we made frequency-switching observations with 9-level sampling and 12.5 MHz bandwidth over 4096 spectral channels in each window to achieve a high velocity resolution of $v_{ch} \approx 0.0386$ km s^{-1} at 23.69 GHz. B1-E1 to B1-E8 were observed for ~ 1120 seconds, each. B1-E9 was observed for ~ 840 seconds.

The GBT data were reduced using standard procedures in GBTIDL[4] for frequency-switched data. In brief, individual scans from each spectral window were filtered for spikes or baseline wiggles, folded, and then averaged. Baselines were obtained for the averaged spectra by fitting 5th-order polynomials to line-free channel ranges at the low- and high-frequency edges of each band, and were then subtracted. To improve the detection levels, the data were smoothed with a boxcar kernel equal to two channels in width. The reduced data were exported from GBTIDL into standard FITS files using routines of AIPS^{++} developed by G. Langston. Further analysis was conducted in MIRIAD[5] and IDL (Interactive Data Language). The 1 σ noise levels were typ-

---

[1] By default, *scanamorphos* sets a much smaller pixel scale.

[2] Due to the fast scan rate, the 160 μm beam is slightly elongated along the scan direction. Thus, we adopt the geometric mean (i.e., $r = \sqrt{ab}$) as the beam size, where the elongated beam dimensions are from Poglitsch et al. (2010).

[3] The GBT is an 100 m telescope operated by the National Radio Astronomy Observatory.

[4] GBTIDL is a special IDL package specific to the GBT.

[5] Multichannel Image Reconstruction, Interactive Analysis, and Display (MIRIAD) software is developed by the Berkeley Illinois Maryland Array (BIMA) group. See Sault et al. (1995) for more details.
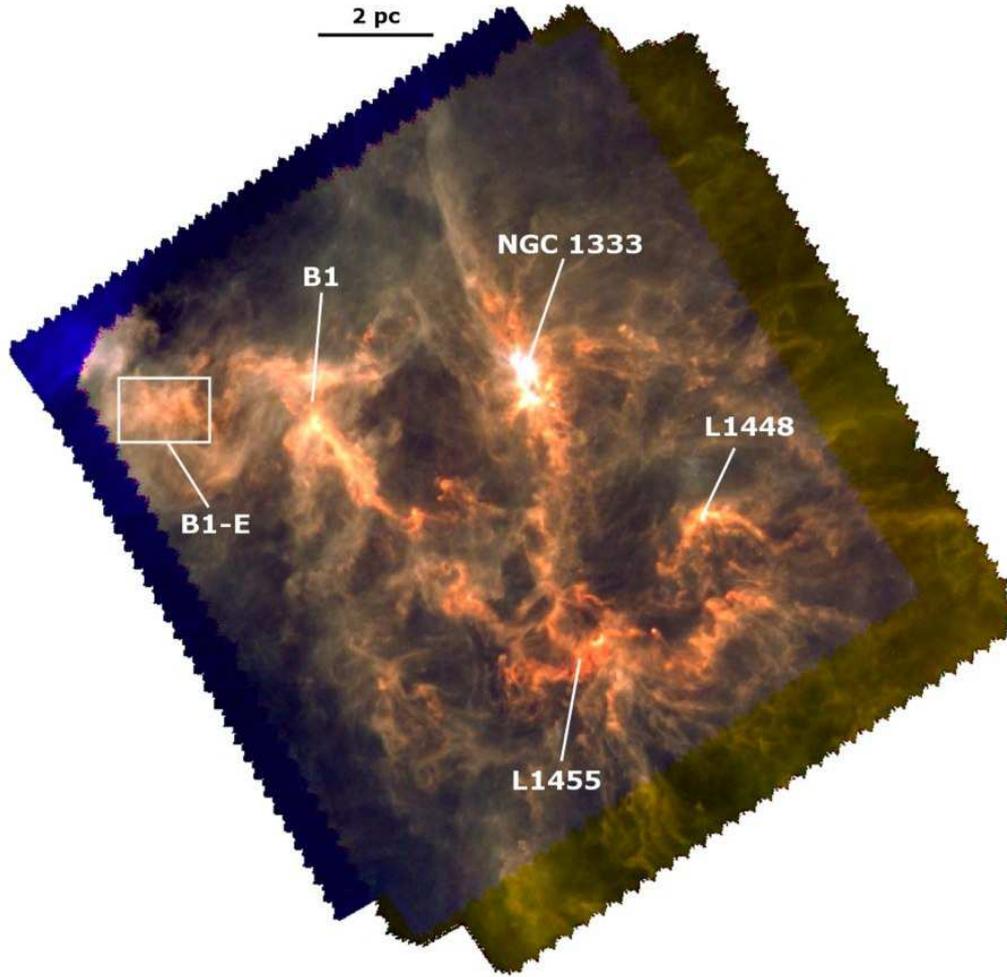
Fig. 1. Three-colour image of the western half of the Perseus molecular cloud. Colour mosaic was generated using *Herschel* 160 μm, 250 μm, and 350 μm observations. The white box denotes our boundary for B1-E for subsequent figures. The other prominent clumps in Perseus are also labeled.
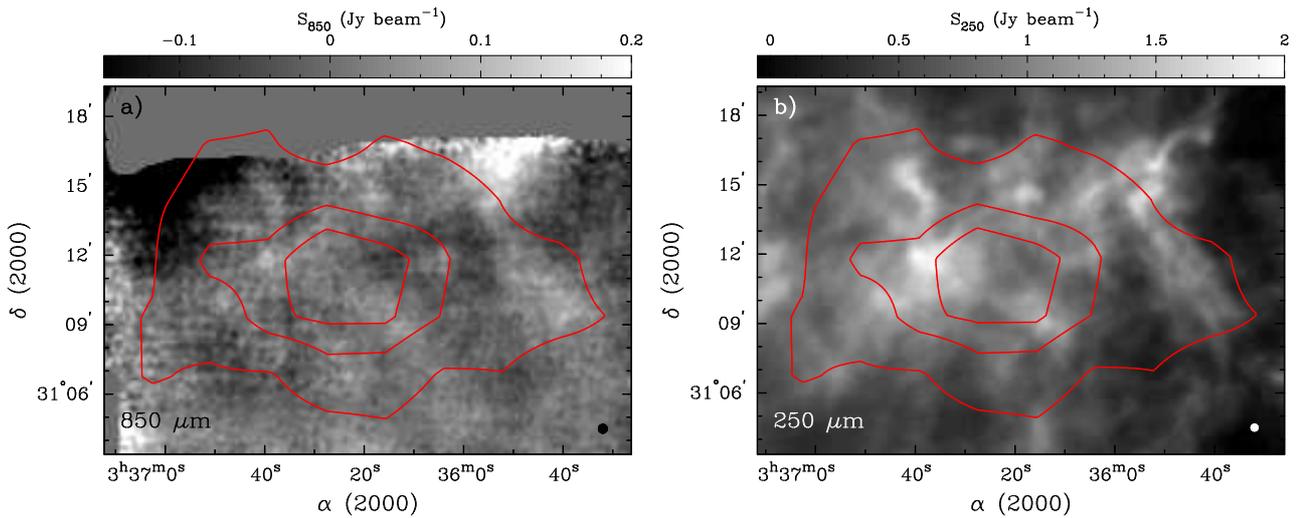

Fig. 2. Observations of Perseus B1-E from (a) SCUBA 850 μm and (b) SPIRE 250 μm maps. The SCUBA data came from the Extended SCUBA Legacy Catalogue (see Di Francesco et al. 2008). Contours represent extinction levels of $A_V = 5, 7, 8$ magnitudes from the COMPLETE extinction map (Ridge et al. 2006a) and the filled circles show the beam sizes of 23″ for smoothed SCUBA data at 850 μm and 18″ for SPIRE data at 250 μm.

ically $\sim 0.01 - 0.02$ K. At 23.69 GHz, the GBT beam is $\sim 33''$ and the beam efficiency is $\eta_b = 0.825$.

Table 1 gives the positions, peak H_2 column density, and the detected line emission of these targets. NH_3 (1,1) line emission was detected ($> 3\,\sigma$) towards all nine targets and CCS ($2_1 - 1_0$) line emission towards several. The NH_3 (2,2) and HC_5N (9-8) lines were only detected toward B1-E2.

3. Results

3.1. SED Fitting to Herschel Data

We corrected the arbitrary zero-point flux offset in each *Herschel* band using the method proposed in Bernard et al. (2010) that is based on a comparison with the Planck HFI (DR2 version, see Planck HFI Core Team et al. 2011) and IRAS data. In addition, each map was convolved to the resolution of the 500 μm map (36.6'') and regridded to 14'' pixels. The map intensities of the $160 - 500\ \mu$m bands were then fit by the modified black body function,

$$I_\nu = \kappa_\nu B_\nu(T)\Sigma \tag{1}$$

where κ_ν is the dust opacity, B_ν is the black body function, T is the dust temperature, and Σ is the gas mass column density. Note that $\Sigma = \mu m_H N(H_2)$, where μ is the mean molecular weight, m_H is the hydrogen mass, and $N(H_2)$ is the gas column density. For consistency with other papers in the Gould Belt Survey (e.g., André et al. 2010),

$$\kappa_\nu = 0.1(\nu/1000\ \text{GHz})^\beta\ \text{cm}^2\ \text{g}^{-1}, \tag{2}$$

where β is the dust emissivity index. The SED fits were made using the IDL program *mpfitfun* by C. B. Markwardt. In brief, *mpfitfun* performs a least-squares comparison between the data and a model function by adjusting the desired parameters until a best fit is achieved.

Fitting β requires a plethora of data, particularly along the Rayleigh-Jeans tail (e.g., $\lambda > 300\ \mu$m at 10 K), to remove degeneracies in the model fits (Doty & Leung 1994; Shetty et al. 2009). Since we have only two photometric bands (350 μm and 500 μm) along the Rayleigh-Jeans tail, we assume $\beta = 2$, consistent with the adopted β in other *Herschel* first-look studies (e.g., André et al. 2010; Arzoumanian et al. 2011). There is some evidence for $\beta \approx 2$ in recent Planck studies (see Planck Collaboration et al. 2011a,b, and references therein). Adopting $\beta = 2$ here provides good fits to our data (see below).

Figure 3 shows the dust temperatures and column densities across B1-E resulting from the modified black body fits to each pixel for the $160 - 500\ \mu$m bands, assuming flux uncertainties of 15% based on calibration uncertainties (see Griffin et al. 2010; Poglitsch et al. 2010) and $\beta = 2$. Both temperature and column density in B1-E are highly structured (see Figures 3a and 3b), where regions of higher column density are also associated with slightly cooler temperatures and regions of lower column density have slightly warmer temperatures. Most of the cooler, high column density material ($\gtrsim 6 \times 10^{21}$ cm^{-2}) is clumped into a central ring-like structure (i.e., slight depression is seen towards the very centre).

Figures 3c and 3d show the number histograms of temperature and H_2 column density, respectively. These distributions are non-Gaussian. The sample mean and standard deviation about the mean for the temperature and column density are 14.1 K±0.8

K and $(6.3 \pm 2.7) \times 10^{21}$ cm^{-2}, respectively, where the standard deviation is computed from,

$$SE = \sqrt{\frac{1}{N-1}\sum(x_i - \bar{x})^2}, \tag{3}$$

where $\bar{x}$ is the population mean for the sample of size N.

These mean values agree well with previously estimated quantities for this region. For example, Schnee et al. (2005) measured a mean dust temperature of ~ 14 K for the B1-E region using the ratio of IRAS 60 μm and 100 μm flux densities to estimate dust temperature. Additionally, extinction data from the COMPLETE survey (see contours in Figures 2 and 3) suggest a mean column density of $(5.3 \pm 1.5) \times 10^{21}$ cm^{-2}, assuming $N(H_2)/A_V = 10^{21}$ cm^{-2} mag^{-1}. Using a higher resolution extinction map from S. Bontemps, we find a mean column density of $(6.3 \pm 3.6) \times 10^{21}$ cm^{-2}. These two column densities agree very well with our measured value of $(6.3 \pm 2.7) \times 10^{21}$ cm^{-2} and they are also similar to the threshold column density for dense core formation from the extinction analysis in Perseus by Kirk et al. (2006), 5×10^{21} cm^{-2}. For comparison, Figure 3d includes the Kirk et al. column density threshold as a dashed line. Although B1-E does not appear filamentary, there is ample material from which dense cores may form. With higher resolution data, André et al. (2011) found a threshold column density of 7×10^{21} cm^{-2} for dense structures to form in Aquila via thermal instabilities along a filament at 10 K.

3.2. Column Density Profiles

One of the more prominent core models is the Bonnor-Ebert sphere (Bonnor 1956; Ebert 1955), which represents the density profile of a sphere in hydrostatic equilibrium under the influence of an external pressure. The Bonnor-Ebert sphere has a flat inner density distribution and a power-law density downtrend at larger radii. Many prestellar cores, i.e., dense cores that are gravitationally bound but do not show evidence of a central luminous protostar, have shown Bonnor-Ebert-like profiles (e.g., Ward-Thompson et al. 1999; Alves et al. 2001).

With the excellent spatial resolution of *Herschel*, we can measure the column density profiles for individual B1-E substructures. First, we identified the *locations* of peak column density using the 2D Clumpfind algorithm (Williams et al. 1994). Briefly, Clumpfind identifies intensity peaks and then uses closed contours at lower intensity levels to assign boundaries. We will discuss the nine highest column density substructures identified by Clumpfind (B1-E1 to B1-E9) for this paper. Second, we measured the azimuthally-averaged column density profile of our nine sources using the *ellint* task in MIRIAD. For simplicity, we used circular annuli of 10'' width for $r > 7''$. For the central radii ($r < 7''$), we assume the peak column density. We caution that several of our sources appear elliptical and our circular approximation is meant to provide a broad, first-look analysis.

Figure 4 shows the column density profiles, where the column density values are plotted from the centre of each annulus. For comparison, Figure 4 also shows the beam profile (solid grey curve), a "generic" column density profile convolved with the beam (dashed grey curve) and an analytical Bonnor-Ebert profile convolved with the beam (dotted curve). For both analytic profiles, we follow the approximation from Dapp & Basu (2009) and assume a temperature of $T = 10$ K, a central density of $n = 10^6$ cm^{-3} and a constant of proportionality of $k = 0.54$, where $k \approx 0.4$ for a singular isothermal sphere and $k \approx 1$

Table 1. GBT Target Information

Source	α (J2000) (h:m:s)	δ (J2000) (° ′ ″)	Peak $N(H_2)^a$ (10^{21} cm^{-2})	Detections[b]
B1-E1	3:35:55.0	31:14:16	18.5	NH_3 (1,1), CCS ($2_1 - 1_0$)
B1-E2	3:36:04.4	31:11:47	16.7	NH_3 (1,1), NH_3 (2,2), CCS ($2_1 - 1_0$), HC_5N (9-8)
B1-E3	3:35:52.1	31:15:39	15.1	NH_3 (1,1), CCS ($2_1 - 1_0$)
B1-E4	3:35:51.0	31:12:34	14.9	NH_3 (1,1)
B1-E5	3:36:37.3	31:11:41	14.5	NH_3 (1,1)
B1-E6	3:36:41.0	31:15:05	13.7	NH_3 (1,1)
B1-E7	3:36:39.0	31:14:27	13.6	NH_3 (1,1), CCS ($2_1 - 1_0$)
B1-E8	3:36:05.0	31:14:28	13.1	NH_3 (1,1), CCS ($2_1 - 1_0$)
B1-E9	3:36:18.5	31:14:31	12.9	NH_3 (1,1)

Notes. [a] Peak *Herschel*-derived H_2 column density towards the sources. See Section 3 for more details. [b] Line emission detected towards each source.
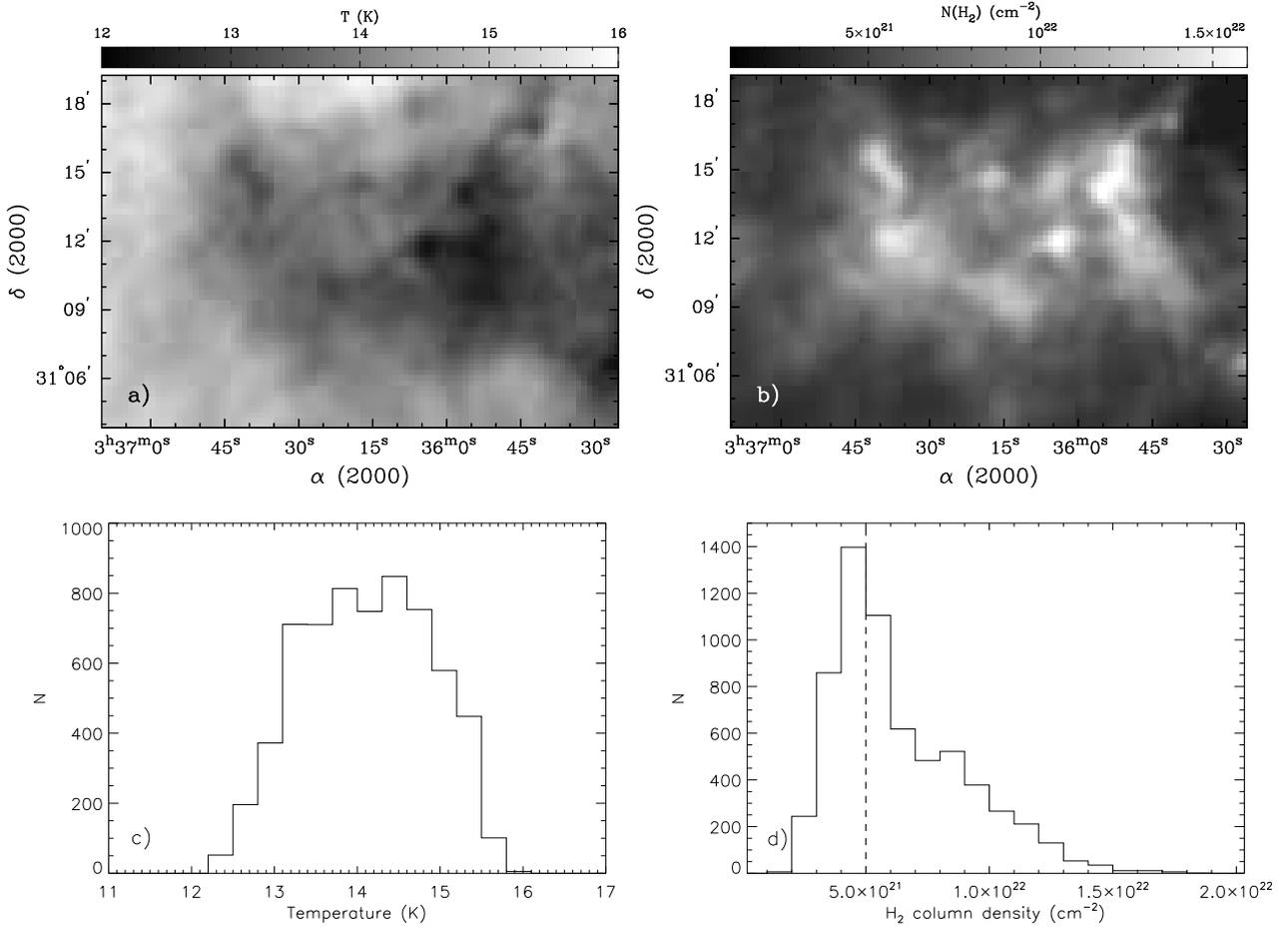

Fig. 3. SED-fitting results for B1-E. *Top panels* shows the temperature (a) and H_2 column density (b) maps across B1-E as measured from SED-fitting to 160 - 500 μm data, according to Equations 1 and 2 and assuming $\beta = 2$. *Bottom panels* show the histograms of the above maps. The temperature histogram (c) uses a bin size of 0.3 K and the H_2 column density histogram (d) uses a bin size of 1×10^{21} cm^{-2}. For comparison, the dashed line in panel (d) indicates the observed column density threshold (from extinction) for core formation from Kirk et al. (2006).

for a collapsing cloud. Our observed column density profiles are much wider than the models, likely due to contaminating material in the foreground or far-background along the line of sight, hereafter called LOS material. Towards the centre of each source, the analytic models and observed profiles are more similar, since the source column density dominates over the LOS level, whereas in the power-law roll-off, the LOS material is likely more significant and the profiles deviate from the analytic models. Unfortunately, the column density of such extended material is difficult to distinguish from the source column density. To estimate its contribution towards each source, we used the subsequent column density at the location where the power-law

slope in the column density profile flattened or began to increase. Thus, the LOS material level ranges from $\sim 8 \times 10^{21}$ cm^{-2} for B1-E9 to $\sim 11 \times 10^{21}$ cm^{-2} for B1-E1 or roughly 60% of the peak column density. These LOS column densities are very conservative and could overestimate their actual contributions by as much as a factor of 2. Indeed, these values are larger than the mean B1-E column density of 6.3×10^{21} cm^{-2}.

Figure 5 shows a comparison of our nine column density profiles after correcting each profile for LOS material and normalizing to the respective peak column density, and includes the Bonnor-Ebert profile, generic profile, and beam profile from Figure 4. All nine profiles follow a shape similar to those of the analytic models, with a flat centre and steep falloff towards larger radii. Additionally, all profiles but B1-E5 generally appear more centrally concentrated than the models, implying that B1-E5 is the least compact. The column density profiles do show some differences with the models, however, such as steeper fall-offs.

3.3. Substructures

We estimated source sizes and masses based on Gaussian fits to the LOS-subtracted column density profiles. Source size was defined by the FWHM of the Gaussian (i.e., R = FWHM/2). Since B1-E6 and B1-E7 have a small projected separation of $\sim 50''$, we truncated both to $31''$ radii[6] to ensure that we mostly measured column densities unique to each. Thus, our analyses of B1-E6 and B1-E7 are biased toward the denser, central regions unlike those of the other sources. Subtracting out the LOS material limits the influence from nearby extended material and generally fits only the denser, embedded object. If we include the LOS material, the estimated source sizes generally increase by $\lesssim 20\%$. Isolated substructures, like B1-E2 or B1-E8, have sizes that vary by $\sim 5\%$ and substructures embedded in extended profiles like, B1-E1 or B1-E4, have sizes that vary by 24% and 37%, respectively.

Table 2 lists the adopted properties for our sources, including their deconvolved radii, estimated (upper and lower) masses, and average densities, assuming they are perfect spheres and dividing the (upper and lower) source masses with their spherical volumes, $\frac{4}{3}\pi R_d^3$, where R_d is the deconvolved radius. We consider two mass and density limits: the lower limits subtract out the LOS material and the upper limits include the LOS material. Note that, by our definition of source size, we are measuring the inner regions of each profile where core precursors are most likely to arise. Since we are using the Gaussian FWHM to estimate the source size, the true source sizes, including any diffuse envelopes, may be larger by a factor of 2. Source mass was estimated by summing over the column density and assuming a mean molecular weight of $\mu = 2.33$. These results provide a reasonable first look at the *relative* sizes and masses of these sources.

3.4. Line Emission

Kirk et al. (2007) and Rosolowsky et al. (2008) each attempted to identify dense gas towards B1-E via high spatial resolution line observations in N$_2$H$^+$ and NH$_3$, respectively. They observed several "blind" pointings towards B1-E and found no strong detections. Unlike previous continuum studies, our *Herschel* data have identified several cold, dense substructures in B1-E (see Figure 3) and these were not directly probed by either Kirk et al. or Rosolowsky et al. Using our *Herschel* results, we se-

---

[6] Deconvolved radii are $\approx 25''$.

Table 2. Column Density Determined Properties

Source	$R_d{}^a$	M^b	n^c
	(AU)	(M$_\odot$)	(10^4 cm^{-3})
B1-E1	7.1×10^3	$0.6 - 1.6$	$5.9 - 17$
B1-E2	6.9×10^3	$0.6 - 1.4$	$6.7 - 15$
B1-E3	7.7×10^3	$0.5 - 1.5$	$4.0 - 12$
B1-E4	6.0×10^3	$0.3 - 1.0$	$4.3 - 18$
B1-E5	9.3×10^3	$0.5 - 2.0$	$2.4 - 9.1$
B1-E6^d	5.9×10^3	$0.3 - 1.0$	$5.7 - 17$
B1-E7^d	5.9×10^3	$0.3 - 0.9$	$5.6 - 17$
B1-E8	7.2×10^3	$0.3 - 1.2$	$3.1 - 12$
B1-E9	5.4×10^3	$0.3 - 0.8$	$5.8 - 18$

Notes. $^{(a)}$ Object radii were estimated from Gaussian fits to the column density profile (R = FWHM/2). Radii were deconvolved with a $36.6''$ beam. $^{(b)}$ Masses are taken from integrating out the column density profiles. The lower limit measurements subtract the LOS material from the column density profiles. The upper limit measurements do not subtract the LOS material from the column density profiles. $^{(c)}$ Average density determined from the mass and volume. $^{(d)}$ B1-E6 and B1-E7 are truncated to measure column density *unique* to each source.

lected the nine substructures with the highest column densities for follow-up observations with the GBT in NH$_3$ (1,1), NH$_3$ (2,2), CCS ($2_1 - 1_0$), and HC$_5$N (9-8) line emission. Figure 6 shows the locations of our nine targets (see also Table 1).
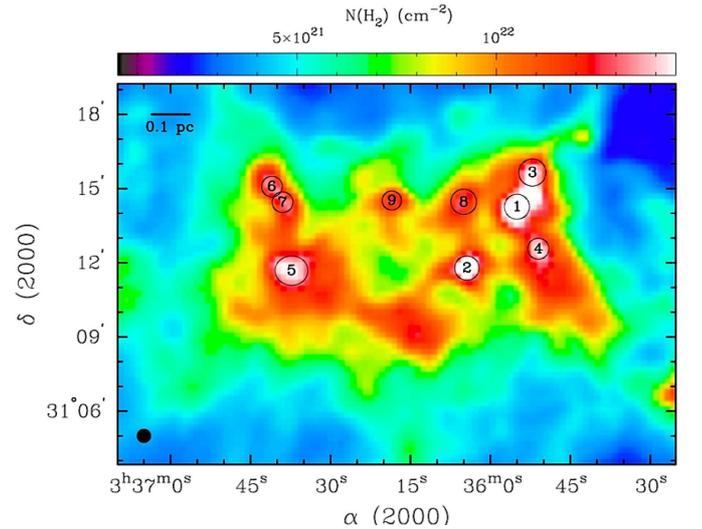

Fig. 6. Locations of substructures in B1-E overlaid on our *Herschel*-derived column density map. Numbers indicate the positions of peak column densities and the relative magnitude of the column density peak (see also Table 1). The thin black circles show the deprojected source sizes (see Section 3.3). The dark filled circle shows the GBT beam ($\sim 33''$) at 23.69 GHz.

3.4.1. NH$_3$

We detected NH$_3$ (1,1) emission towards all nine targets. We fit the NH$_3$ (1,1) hyperfine lines with multiple Gaussian components using the following equation;

$$\tau(v) = \tau_{1,1} \sum_{i=1}^{18} \alpha_i \exp\left[-4 \ln 2 \left(\frac{v - v_i - v_{lsr}}{\Delta v}\right)^2\right] \qquad (4)$$
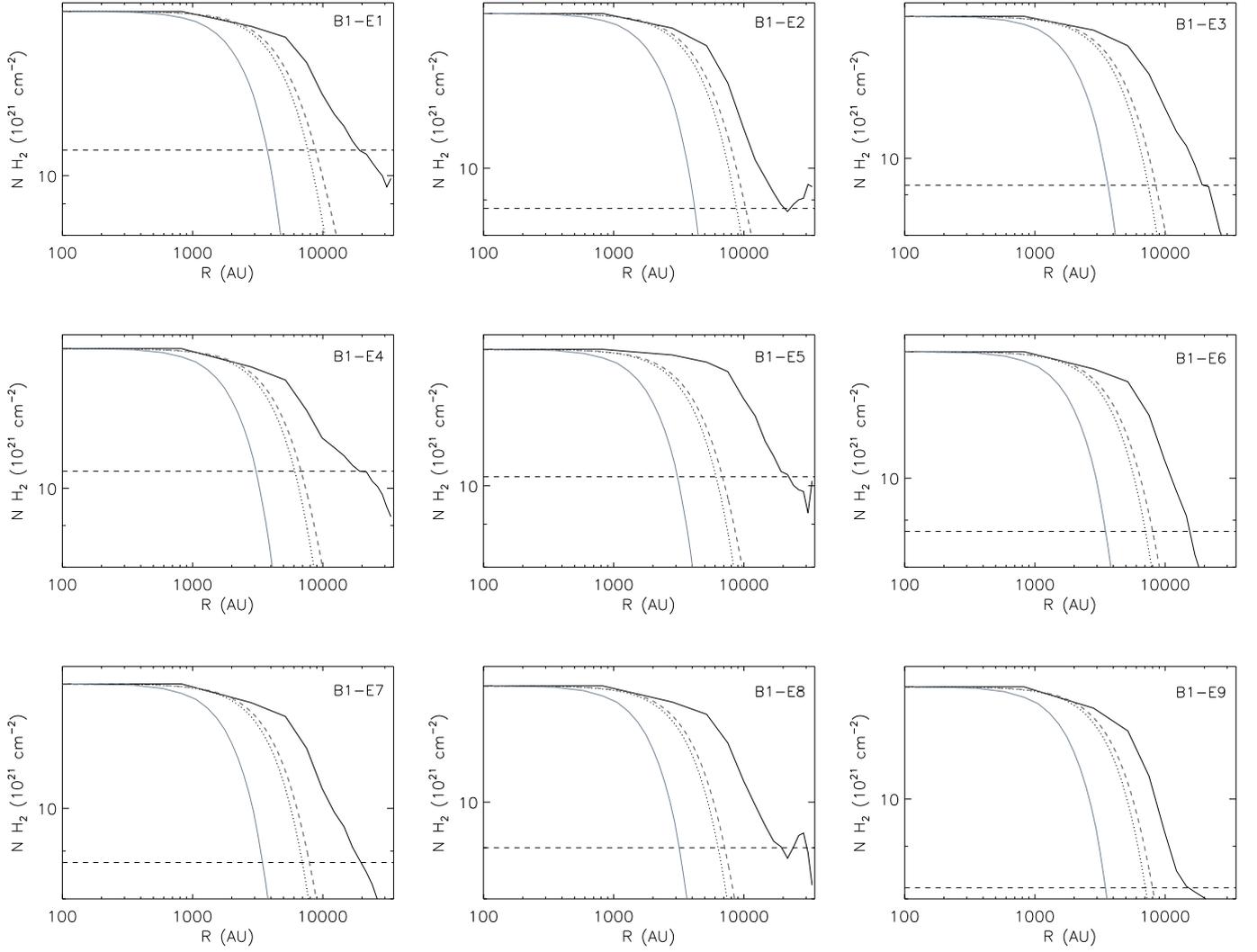
Fig. 4. The azimuthally-averaged column density profiles for the nine sources in B1-E, assuming a distance of 235 pc. The profiles were measured using circular annuli with a thickness of $10''$ for $r > 7''$. Note that the central area is defined by a circle of radius $7''$ but plotted at $3.5''$. The dashed line indicates our estimate for the non-source line-of-sight (LOS) material. For comparison, the dotted curve and dashed curve illustrate a Bonnor-Ebert column density profile and a "generic" $[1 + (r/a)^2]^{-0.5}$ column density profile following Dapp & Basu (2009). For both analytic curves, we assume a temperature of 10 K and a central density of $n = 10^6$ cm^{-3} and convolved the profiles with a $36.6''$ beam. The grey solid curve shows the beam profile. The analytical profiles and the beam profile are scaled to the peak column density. Note that both axes are logarithmic.

where $\tau_{1,1}$ is the optical depth for the (1,1) transition, α_i is the transition weight, v_i is the velocity of the hyperfine line (for a given rest frequency), v_{lsr} is the velocity of the source with respect to the local standard of rest, and Δv is the FWHM of the line. We used the hyperfine frequencies and weights from Kukolich (1967) and Rydbeck et al. (1977) and derived the values for $\tau_{1,1}$, v_{lsr}, and Δv from the fits. Figure 7 shows example fits to the NH$_3$ spectra. Table 3 lists centroid velocity (v_{lsr}) and *uncorrected* velocity line width (Δv) from the NH$_3$ (1,1) fits, the kinetic gas temperature from NH$_3$ (1,1) and (2,2) line comparisons, and the resulting thermal and non-thermal velocity dispersions for all nine sources.

For B1-E2, we could derive the kinetic gas temperature using NH$_3$ (1,1) and NH$_3$ (2,2) line emission, whereas we could only determine upper limits for our other sources. We use our NH$_3$-derived kinetic temperature of $T_K = 10.26$ K ± 0.36 K for B1-E2 and adopt the mean NH$_3$-derived kinetic temperature of 11 K from the survey of Rosolowsky et al. (2008) for

our other sources. As an estimate of the uncertainty, we use the dispersion in the kinetic temperatures from the Rosolowsky et al. data, 2 K, (see Enoch et al. 2008). Note that these gas temperatures correspond to the denser, colder inner layers where ammonia is excited, whereas the dust temperatures (see Section 3.1) represent an average of all the material along the line of sight, i.e., including the lower density envelopes. For more information on extracting kinetic temperatures from NH$_3$ line emission, see Friesen et al. (2009).

Table 3 also lists the thermal velocity dispersion, σ_T, and the non-thermal velocity dispersion, σ_{NT}. We determined σ_T from the kinetic temperature and σ_{NT} from the line widths via,

$$\sigma_T = \sqrt{\frac{k_b T_K}{\mu_{NH_3} m_H}} \tag{5}$$

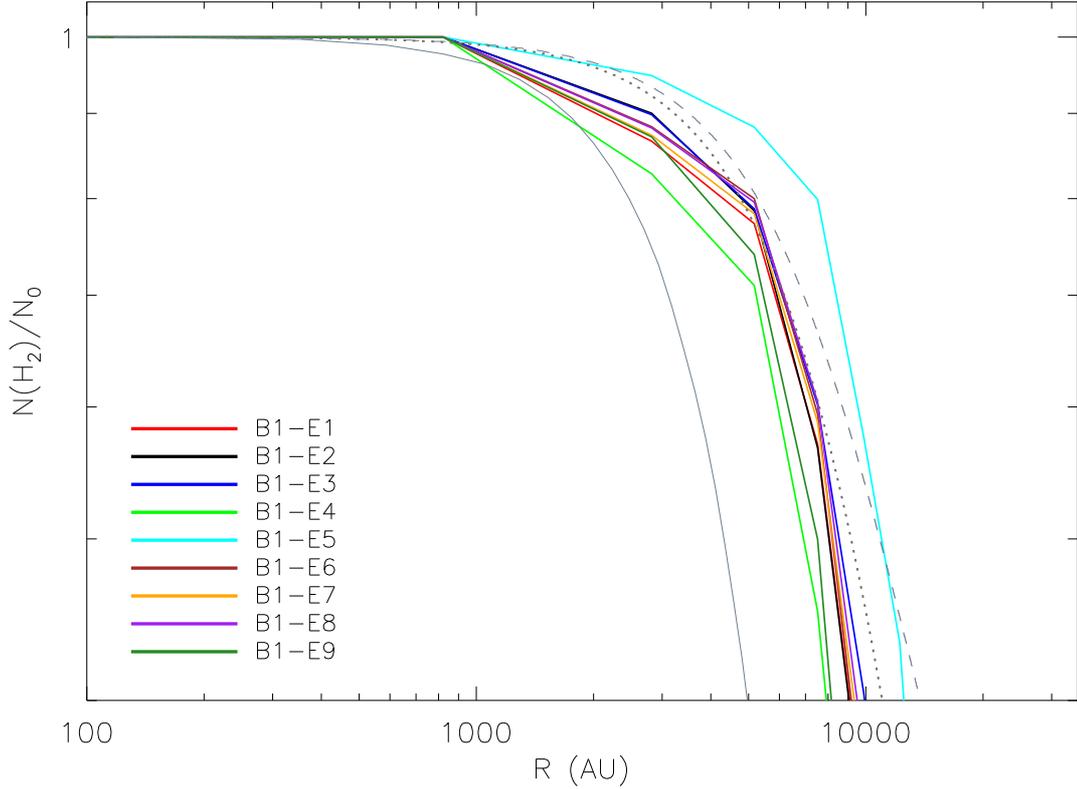$$\sigma_{NT} = \sqrt{\sigma_{obs}^2 - \sigma_T^2}, \tag{6}$$

7

Fig. 5. Normalized column density profiles for sources in B1-E, assuming a distance of 235 pc. Column density was determined from azimuthally-averaged annuli (see Figure 4). Furthermore, the LOS material was estimated for each source and subtracted from the azimuthal average. The grey solid, dotted, and dashed curves are the same as for Figure 4.

Table 3. Properties from NH_3 (1,1) and NH_3 (2,2) Line Spectra

Source	v_{lsr} (km s^{-1})	Δv^a (km s^{-1})	$T_K{}^b$ (K)	$\sigma_T{}^c$ (km s^{-1})	σ_{NT} (km s^{-1})
B1-E1	7.61 ± 0.02	0.998 ± 0.056	< 27	0.073 ± 0.007	0.417 ± 0.025
B1-E2	7.67 ± 0.002	0.293 ± 0.005	10.26 ± 0.36	0.071 ± 0.001	0.101 ± 0.003
B1-E3	7.47 ± 0.01	0.681 ± 0.030	< 16	0.073 ± 0.007	0.280 ± 0.015
B1-E4	7.83 ± 0.01	1.078 ± 0.036	< 27	0.073 ± 0.007	0.451 ± 0.016
B1-E5	7.57 ± 0.01	0.833 ± 0.022	< 19	0.073 ± 0.007	0.344 ± 0.012
B1-E6	7.61 ± 0.01	0.905 ± 0.032	< 23	0.073 ± 0.007	0.376 ± 0.015
B1-E7	7.31 ± 0.01	0.708 ± 0.032	< 24	0.073 ± 0.007	0.290 ± 0.016
B1-E8	6.78 ± 0.01	0.537 ± 0.021	< 20	0.073 ± 0.007	0.213 ± 0.012
B1-E9	7.11 ± 0.01	0.690 ± 0.038	< 32	0.073 ± 0.007	0.282 ± 0.018

Notes. [a] The velocity FWHM from the best-fit models uncorrected for channel resolution. [b] Kinetic temperature towards each source. For B1-E2, we measured the kinetic temperature from NH_3 (1,1) and NH_3 (2,2) line emission. For our other sources, we used a 3 σ upper limit for NH_3 (2,2) to estimate the upper limit of T_K. [c] The thermal line width of B1-E2 was determined using the derived kinetic temperature, $T_K = 10.26$ K ± 0.36 K. For the remaining sources, we adopted 11 K, the mean NH_3-derived kinetic temperature from Rosolowsky et al. (2008) with an uncertainty of 2 K from the dispersion of the kinetic temperature in that survey (see Enoch et al. 2008).

where k_b is the Boltzmann constant, T_K is the kinetic temperature, $\mu_{NH_3} = 17.03$ is the mean molecular weight of NH_3, m_H is the atomic hydrogen mass, and σ_{obs} is the total *corrected* velocity dispersion of the lines, $\sigma_{obs} = \Delta v_c / \sqrt{8 \ln 2}$ for $\Delta v_c{}^2 = \Delta v^2 - v_{ch}^2$. Using the NH_3 study by Rosolowsky et al. (2008), we adopted $T_K = 11$ K for all our targets except B1-E2, where we used our derived gas temperature, $T_K = 10.26$ K ± 0.36 K.

3.4.2. CCS and HC$_5$N

CCS $(2_1 - 1_0)$ was detected towards five targets (see Table 1) and HC$_5$N (9-8) was detected towards only B1-E2. Figure 8 shows examples of these spectra. We fit the CCS $(2_1 - 1_0)$ and HC$_5$N (9-8) spectra with single Gaussians. The velocities determined for most CCS $(2_1 - 1_0)$ detections and the single HC$_5$N (9-8) detection were similar to those found from NH_3, suggesting these dense gas tracers are probing the same region as the NH_3 emission. The CCS $(2_1 - 1_0)$ spectra for B1-E1 and B1-E8, however, revealed fairly different values. For B1-E1, the
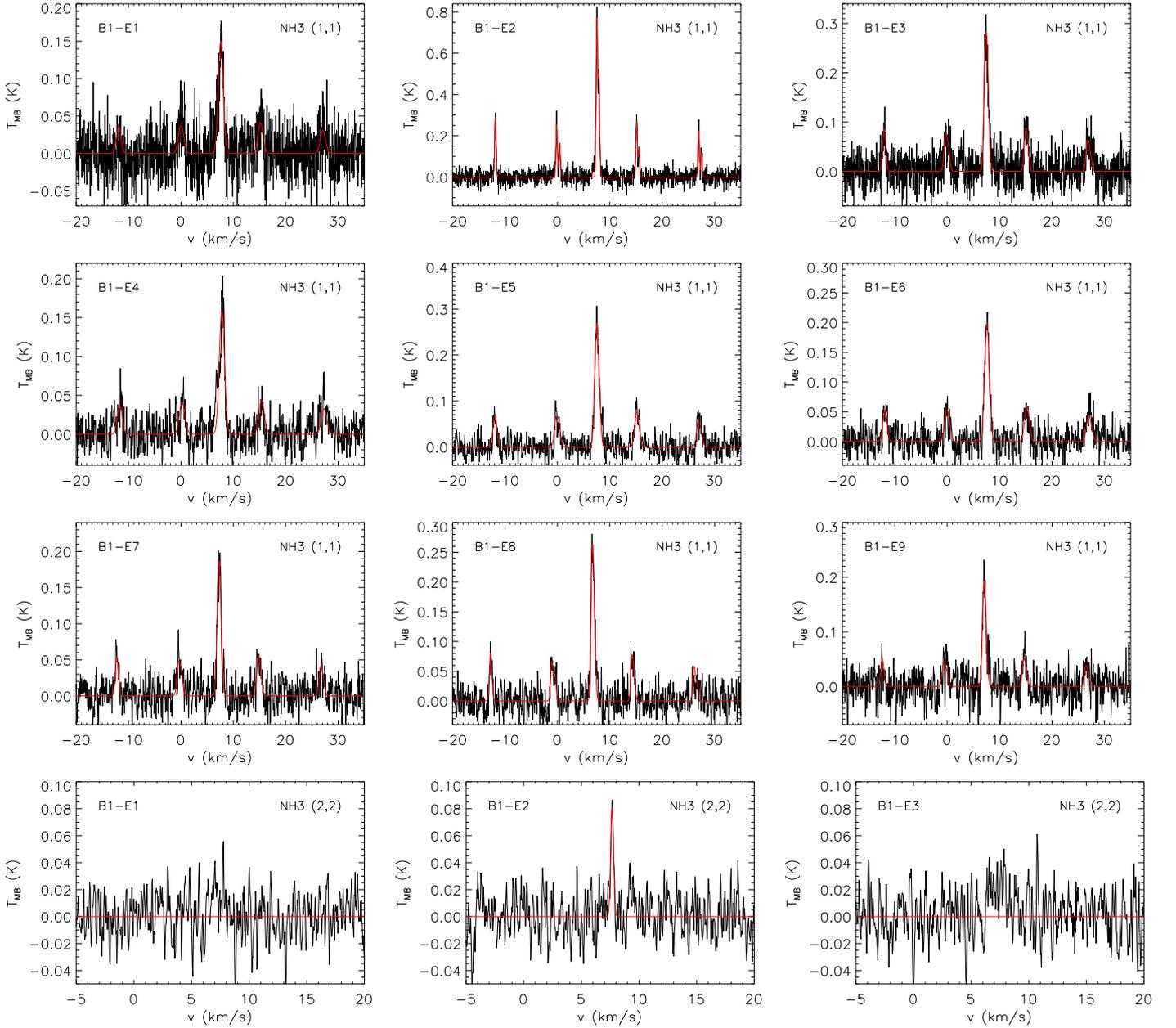
Fig. 7. Fits to NH_3 (1,1) and (2,2) spectra. Note the hyperfine components visible for the NH_3 (1,1) spectrum of B1-E2. The NH_3 (2,2) spectra were smoothed by a boxcar with a 2-channel width to improve the visual appearance. For comparison, we show two undetected NH_3 (2,2) observations.

CCS ($2_1 - 1_0$) line emission appears redshifted by ~ 0.3 km s^{-1} ($15\,\sigma$) with respect to the NH_3 (1,1) line emission, whereas for B1-E8, the CCS ($2_1 - 1_0$) line emission is redshifted by ~ 0.11 km s^{-1} ($2\,\sigma$). The redshifted CCS ($2_1 - 1_0$) emission in B1-E1 may be tracing a different region of dense gas from the NH_3 emission, such as a region undergoing infall (e.g., see Swift et al. 2005). 3

4. Discussion

Our *Herschel* data have revealed extensive substructures within B1-E for the first time. Such faint substructures may represent an early evolutionary stage in star formation, where a first generation of cores is forming from lower density material. Thus, it is important to characterize the substructures seen in these *Herschel* maps.

4.1. Comparison with Jeans Instability

The minimum length scale for gravitational fragmentation in a purely thermal clump or cloud is described by the Jeans length, $\lambda_J = (c_s^2 \pi / G\rho)^{1/2}$, where c_s is the thermal sound speed, G is the gravitational constant, and ρ is the density of material (Stahler & Palla 2005). In terms of temperature and number density, we find,

$$\lambda_J = 0.21 \left(\frac{T}{10\ \mathrm{K}}\right)^{0.5} \left(\frac{n}{10^4\ \mathrm{cm}^{-3}}\right)^{-0.5}\ \mathrm{pc}. \qquad (7)$$

Ideally, the Jeans length should be calculated for the gas temperature and gas density. In small, dense scales (i.e., $\gtrsim 10^5$ cm^{-3}; Di Francesco et al. 2007), the gas and dust temperatures are coupled, whereas in larger, more diffuse scales, the gas and dust are decoupled and the gas may be warmer than the dust (Young et al.
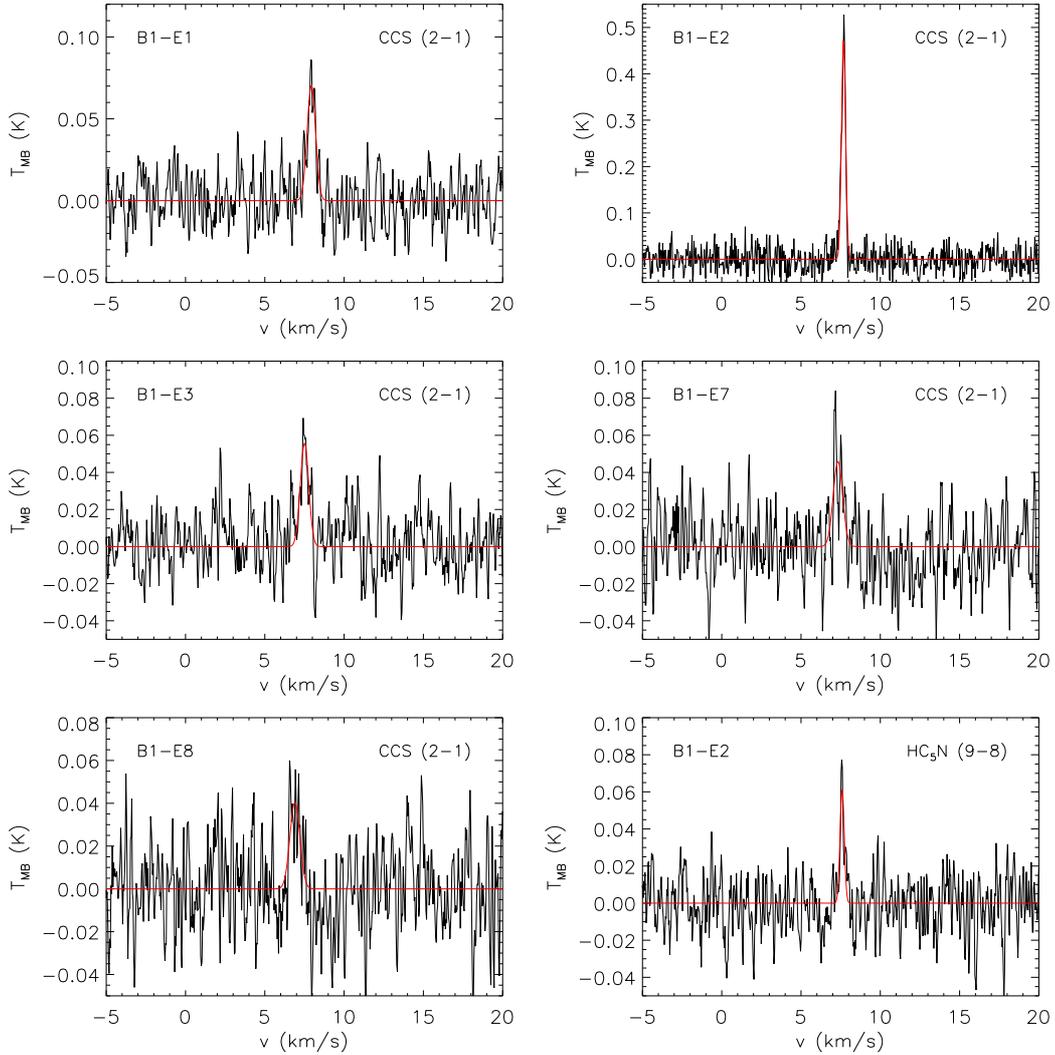
Fig. 8. Fits to the detected CCS $(2_1 - 1_0)$ and HC$_5$N (9-8) spectra. The weaker CCS $(2_1 - 1_0)$ spectra and the B1-E2 HC$_5$N (9-8) spectra were all smoothed by a boxcar with a 2-channel width to improve the visual appearance of the lines. The B1-E2 CCS $(2_1 - 1_0)$ spectrum was not smoothed.

2004; Di Francesco et al. 2007; Ceccarelli et al. 2007). The central region of B1-E containing the substructures, i.e., the area contained within $N(H_2) > 6 \times 10^{21}$ cm^{-2}, has a mass of ~ 110 M$_\odot$ and an effective radius ($R_{eff} = \sqrt{A/\pi}$) of ~ 0.46 pc. Approximating B1-E as a sphere, we find an average density of $\sim 5 \times 10^3$ cm^{-3}, suggesting that the the gas and dust in B1-E are likely decoupled such that the mean dust temperature of ~ 14 K (see Section 3.1) is a lower limit to the gas temperature. Assuming a lower limit gas temperature of 14 K and $n = 5 \times 10^3$ cm^{-3}, the lower limit $\lambda_J \approx 0.35$ pc. Note that the kinetic temperatures measured in Section 3.4.1 correspond to the smaller, denser scales where the gas and dust temperatures should be coupled and not the scales measured here.

The minimum projected separations between our nine substructures are generally between 0.1 pc and 0.19 pc, with a median value of ~ 0.13 pc for all nine sources. Recall, however, that B1-E6 and B1-E7 have an angular separation of ~ 0.05 pc, a factor of 2 closer than any other pair of substructures. Despite their close proximity, B1-E6 and B1-E7 show different centroid velocities (see Table 3), and therefore, cannot be considered a single object. Also, we can only measure the projected 2-D separations between our nine substructures and not their physical

3-D separations. Assuming a typical inclination angle of $60°$, our median separation is ~ 0.15 pc for all nine substructures or ~ 0.17 pc excluding B1-E6 and B1-E7.

The median minimum separation is a factor of two smaller than our best estimate of the Jeans length, though our Jeans length estimate is, itself, uncertain within a factor of a few. The fact that we find a minimum separation that is less than the Jeans length is still interesting and could indicate gravitational fragmentation followed by bulk contraction of the B1-E group, but the overall uncertainties in determining the minimum separations and Jeans length make this difficult to validate. Additionally, B1-E does not appear to be filamentary (see Figure 6) and therefore, the clump could be extended along the line of sight resulting in more significant radial distances between substructures.

For the substructures, we use the Jeans mass to explore their thermal stabilities. Similar to the Jeans length, the Jeans mass is a critical mass scale for gravitational fragmentation (Stahler & Palla 2005). This critical mass can be described as,

$$M_J = 2.9 \left(\frac{T}{10 \text{ K}} \right)^{1.5} \left(\frac{n}{10^4 \text{ cm}^{-3}} \right)^{-0.5} \text{ M}_\odot. \tag{8}$$

The B1-E substructures have average densities of $n \sim 1 \times 10^5$ cm^{-3} (see Section 3.3). Furthermore, we found a gas temperature for B1-E2 of ~ 10 K. Note, that this gas temperature corresponds to the denser B1-E2 substructure and should not be assumed for the lower density B1-E clump. Assuming $T = 10$ K and $n = 1 \times 10^5$ cm^{-3}, the critical Jeans mass is $M_J \approx 0.9$ M$_\odot$. Several of the substructures have mass limits on order of the Jeans mass (see Table 2), suggesting that these sources are approaching a critical, unstable mass. Thus, the B1-E substructures are interesting prospects for future studies of substructures evolution.

4.2. Time Scale for Interactions

From the *Herschel* observations, the B1-E substructures appear linked (see Figure 6), which might indicate that they are interacting. The timescale for any two substructures to interact can be estimated from the typical separation between the substructures and their velocity dispersion. For simplicity, we adopt the average projected separation between all nine substructures of ~ 0.40 pc. For an inclination angle of $60°$, the typical separation between the substructures is $d_{ave} \sim 0.46$ pc. To estimate the velocity dispersion of the sources, we use the dispersion of the centroid velocities of NH$_3$ (1,1) from all nine objects. The weighted 1D centroid velocity dispersion is $\sigma_{1D} \approx 0.24$ km s^{-1} and assuming symmetry, the 3D velocity dispersion[7] is $\sigma_{3D} \approx 0.42$ km s^{-1}. Thus, the B1-E substructures have an interaction timescale of ~ 1 Myr, a factor of two larger than recent estimated prestellar core lifetimes and less than the expected protostellar core lifetime (e.g., Kirk et al. 2005; Ward-Thompson et al. 2007; Enoch et al. 2008). Furthermore, this timescale corresponds to the interaction time between any two substructures and not the interaction time between nearest neighbour substructures. Given that the nearest neighbour separation is a factor of ~ 3 smaller than the typical separation adopted here, these substructures have the potential to interact prior to forming stars. Thus, competitive accretion may be significant during further evolution of B1-E (e.g., Bonnell et al. 2001; Krumholz et al. 2005; Bonnell & Bate 2006).

4.3. Comparison with Virial Equilibrium

Not all dense substructures will form cores and stars. For example, a core with kinetic energy from internal motions that exceeds its gravitational binding energy may be transient and unable to form persistent dense structures or stars. According to McKee (1999), a core is gravitationally bound if the virial parameter, α, is

$$\alpha = \frac{M_{virial}}{M} = \frac{5\sigma_v^2 R}{GM} \lesssim 2 \qquad (9)$$

where σ_v is the velocity dispersion, R is the radius, and M is the mass.

B1-E has an effective radius of 0.46 pc (see Section 4.1). We estimate the velocity dispersion using the centroid velocity dispersion from Section 4.2, $\sigma_{3D} = 0.42$ km s^{-1}. This velocity dispersion was derived from the motions of the individual substructures and thus, reflects the turbulence in the cloud that first created the substructures rather than the thermal velocity dispersion of the gas. The expected thermal velocity of the gas is less than 0.42 km s^{-1}, and thus non-thermal support is important. Assuming $R = 0.46$ pc and $\sigma_v = 0.42$ km s^{-1}, B1-E has a

---

[7] Assuming $\sigma_{3D}^2 = \sigma_r^2 + \sigma_\phi^2 + \sigma_\theta^2 = 3\sigma_r^2$.

Table 4. Virial Analysis Properties

Source	σ_v (km s^{-1})	σ_v/c_s[a]	M_{virial} (M$_\odot$)	α[b]
B1-E1	0.461 ± 0.030	2.3 ± 0.3	8.5 ± 4.8	5 - 14
B1-E2	0.216 ± 0.005	1.1 ± 0.03	1.8 ± 0.9	1 - 3
B1-E3	0.342 ± 0.022	1.7 ± 0.2	5.1 ± 2.9	3 - 10
B1-E4	0.492 ± 0.022	2.5 ± 0.3	8.2 ± 4.5	8 - 27
B1-E5	0.397 ± 0.018	2.0 ± 0.2	8.3 ± 4.5	4 - 17
B1-E6	0.424 ± 0.022	2.1 ± 0.2	6.0 ± 3.3	6 - 20
B1-E7	0.351 ± 0.023	1.8 ± 0.2	4.1 ± 2.3	5 - 13
B1-E8	0.291 ± 0.021	1.5 ± 0.2	3.4 ± 2.0	3 - 11
B1-E9	0.344 ± 0.025	1.7 ± 0.2	3.6 ± 2.1	5 - 12

Notes. [a] Velocity dispersion divided by sound speed, assuming $T = 11$ K for all substructures except B1-E2 where $T = 10.23$ K. [b] Virial parameter considering the upper and lower mass limits for each substructure (see Table 2).

---

virial mass of ~ 96 M$_\odot$, or $\alpha \approx 0.9$ for a clump mass of 110 M$_\odot$ (see Section 4.1). These results imply that B1-E is itself gravitationally bound and thus, likely to form dense cores and stars in the future.

For the individual substructures, velocity dispersions were determined from NH$_3$ (1,1) line widths, after estimating the non-thermal component (σ_{NT}; see Table 3) and the thermal component (c_s) for a mean molecular weight of $\mu_{H_2} = 2.33$. Table 4 shows our values for the total velocity dispersion, σ_v, the ratio of the velocity dispersion to the thermal sound speed, the virial mass, M_{virial}, and the virial parameter, α, for each substructure. Most of the virial parameters are $\gg 2$, suggesting that these substructures themselves are not gravitationally bound and thus, may not necessarily represent persistent objects. B1-E2 has the smallest virial parameter, $1 \lesssim \alpha \lesssim 3$, however, and may be itself gravitationally bound. B1-E8 and B1-E3 have lower limit estimates of $\alpha \sim 3$ and given that we know α only within a factor of a few, these sources may also be gravitationally bound. These virial limits, however, depend greatly on the source mass, which can vary by a factor of ~ 4 depending on our treatment of the LOS material (see Section 3.3). To be bound, these candidates must have negligible LOS material towards them, which is very unlikely. Thus, B1-E2 is the only strong candidate for being gravitationally bound.

Most B1-E substructures have very large virial parameters and are thus, expected to be unbound. In comparison, the Jeans mass (see Section 4.1) is a mass scale for only gravitational fragmentation in a thermal clump and does not include the contributions from non-thermal support. Several of the substructures with $\alpha \gg 2$ have masses on order of the Jeans mass, ~ 0.9 M$_\odot$, suggesting that the Jeans mass analysis is too simplistic and does not well represent the evolutionary state of these structures. For example, the substructures may have significant turbulent motions. With only one potentially bound substructure (B1-E2), it is difficult to determine if B1-E will eventually form several cores or no cores at all (i.e., these substructures are all transient).

The substructures themselves show large line widths (see Table 4), atypical of dense prestellar cores, which are subsonic. In particular, B1-E2 has the narrowest line profiles (by at least a factor of 2) and the strongest line detections, suggesting that this object is the most evolved of the substructures. These observations hint at a possible dynamic evolution, where dense cores first contain significant non-thermal, turbulent motions which dissipate into coherent, quiescent dense cores. If so, the substructures in B1-E may become more bound over time as their

turbulent support is dissipated, a process which may explain the narrower lines toward B1-E2.

Note that we assume $T_K = 11$ K for our substructures (except B1-E2). In Section 3.4.1, we found upper limits for kinetic temperature > 11 K (see Table 3). Furthermore, we are using a simplified virial equation in Equation (9). Ideally, the virial equation includes magnetic pressure and surface pressure terms which can either assist gravity in the collapse or help in the support of a clump (e.g., see Nakamura & Li 2008). Our observations, however, do not measure these quantities and thus, we use a simplified virial equation. Nevertheless, B1-E2 is special with respect to the other substructures. Indeed, we may have the first observations of a core precursor.

4.4. Comparison with Other Star Forming Regions

B1-E has column densities well above $\sim 5 \times 10^{21}$ cm^{-2}, the core formation threshold reported by Kirk et al. (2006). Since the other clumps with similarly high column densities are actively forming stars, it is reasonable to expect B1-E to do the same in the near future. Furthermore, Lada et al. (2010) found a good correlation between the number of YSOs in a cloud (or clump) with the cloud mass above $A_K > 0.8$ (or $A_V > 7.3$) for several star forming regions. Based on their extinction threshold, we find a clump mass of ~ 90 M$_\odot$ for N(H$_2$) > 7.3×10^{21} cm^{-2} and thus, we could expect ~ 10 YSOs to form in B1-E. With *Herschel*, we have detected several substructures with moderate densities of $\sim 10^5$ cm^{-3} (see Table 2), similar to what is often defined for dense cores, i.e., $\gtrsim 10^4$ cm^{-3} (Bergin & Tafalla 2007).

These substructures, however, were not well observed by SCUBA at 850 μm or Bolocam at 1 mm (see Figure 2), and thus, are not dense cores in the traditional definition. The substructures in B1-E also have supersonic velocity dispersions. In general, low-mass starless cores have subsonic velocity dispersions (e.g., Myers 1983; Kirk et al. 2007; André et al. 2007; Pineda et al. 2010) whereas protostellar cores can have supersonic velocity dispersions (e.g., Gregersen et al. 1997; Di Francesco et al. 2001). Since we see no evidence of protostellar activity whatsoever (i.e., from *Spitzer* data), these substructures are likely unevolved.

Thus, the substructures in B1-E are likely core precursors and more observations of this region should provide some insight into core formation (transient or persistent) in molecular clouds. In particular, B1-E is isolated from YSOs and young stars, so the region is unaffected by environmental processes such as outflows or winds. A nearby expanding dust shell, seen in IRAS 60 μm and 100 μm data (Ridge et al. 2006b), may be sweeping material towards B1-E, though the ring itself does not appear to be directly interacting with this clump. This shell may have a larger impact on the evolution of structure in B1-E in the future.

A relatively pristine core forming region is exceedingly rare. The only additional case may be the inactive high extinction clump (211) identified in L1495 by Schmalzl et al. (2010), though further detailed studies of that clump are still necessary to determine what, if any, substructures are forming cores and stars. A collection of starless cores in Aquila form a similar grouping as in B1-E, however this region has two known protostars nearby ($\lesssim 1$ pc) and so is not as pristine as B1-E (Könyves et al. 2010, see their Figure 5).

4.5. Comparison with Core Formation Models

Core formation simulations attempt to recreate molecular cloud fragmentation, implementing factors such as gravitational collapse, magnetic pressure, and turbulent energy. Many recent studies have argued that models of core formation must consider both ambipolar diffusion and turbulence (e.g., Li & Nakamura 2004; Dib et al. 2007; Nakamura & Li 2008; Basu et al. 2009a,b; Gong & Ostriker 2011). Magnetic fields introduce an additional pressure support that opposes gravitational collapse, whereas turbulence either opposes collapse by introducing kinetic energy support or induces collapse via energy dissipation from compressive shocks.

Several recent studies have examined the effects of different magnetic field and turbulent flow properties (e.g., Li & Nakamura 2004; Basu et al. 2009a; Price & Bate 2009). In particular, these simulations examine fragmentation in subcritical (where magnetic fields dominate over gravity) and supercritical (where gravity dominates over magnetic fields) regimes with dissipating turbulent flows. In the *subcritical* simulations, the fragmenting clouds generally form cores in relative isolation and with less filamentary morphologies, such as ring-like distributions of loose core groups (see also Li & Nakamura 2002). These cores tend to form more slowly, i.e., fragmentation is suppressed by the strong magnetic field, and since large-scale turbulent flows are generally damped, the velocity field is generally subsonic. (Note that Basu et al. 2009a, find that strong magnetic fields can induce oscillations and create a supersonic velocity field, i.e., $\lesssim 3c_s$.) In contrast, *supercritical* simulations generally form cores associated with filaments, and these cores tend to form relatively quickly and can move supersonically through their environment.

An isolated core forming region is necessary to test model predictions and constrain initial conditions of dense gas before the onset and influence of nearby stars and internal protostars. Thus, B1-E is an ideal target for such measurements (see Section 4.4). From our observations, B1-E contains a small, loose grouping of substructures. Although the substructure morphology observed in B1-E is not entirely ring-shaped, the distribution hints at an inclined ring-like structure. Furthermore, if star formation is triggered, it is surprising that B1-E, which is bookended by two highly active and more evolved clumps, IC 348 to the far east and NGC 1333 to the far west, contains no evidence for evolved star formation itself. Furthermore, IC 348 shows many evolved pre-main sequence stars and NGC 1333, though appearing younger, has many YSOs (Bally et al. 2008; Herbst 2008; Walawender et al. 2008), suggesting that B1-E is not part of an age gradient.

These observations suggest that *B1-E is influenced by a strong, localized magnetic field*. Further tests of this scenario would be possible by observing the entire velocity field for B1-E. Instead, we could only estimate the bulk velocity field from the relative motions of the individual substructures (from line centroids; see Section 4.2), $\sigma_{3D} = 0.42$ km s^{-1}. Additionally, we do not have direct measurements of the gas temperature for the B1-E clump. If we use the mean B1-E dust temperature of 14 K as the lower limit gas temperature, $c_s \gtrsim 0.22$ km s^{-1} and the velocity field within B1-E may be supersonic by $\lesssim 2c_s$. These motions can arise in either subcritical or supercritical clouds, though the latter is generally associated with supersonic velocities.

Direct measurements of the magnetic field would also be useful to constrain its role in B1-E. Unfortunately, very little magnetic field information is available here. Goodman et al. (1990) measured optical polarization towards all of Perseus, and

for B1-E, they found strong, ordered polarization vectors reaching ~ 9% polarized light, a factor of two higher than any other dense region in Perseus. While these polarization observations may suggest a strong magnetic field is associated with the B1-E region, these observations are dependent on the field viewing angle. Also, these data were obtained at very low resolution resulting in only three vectors coinciding with B1-E.

A strong magnetic field does not necessarily relegate turbulent compression or gravity to minor roles in the evolution of B1-E. Indeed, Nakamura & Li (2008) suggest that core forming regions exhibit different phases where magnetic fields, gravity, and turbulence are sometimes dominant and sometimes secondary. For example, they suggest that core forming regions begin with strong magnetic fields and strong turbulence, such that gravity is a secondary effect. After the turbulent energy dissipates, gravitational collapse can proceed via magnetic field lines.

5. Conclusions

With recent *Herschel* dust continuum observations from the *Herschel* Gould Belt Survey, we identified substructure in the Perseus B1-E region for the first time. With our *Herschel* data, we determined the temperature and column density across the region. We selected the nine highest column density substructures for complementary observations with the GBT. We summarize our main conclusions as follows:

1. B1-E contains a loose collection of roughly a dozen prominent substructures. This morphology is atypical of most star forming regions, which produce dense clusters and organize material along filaments. Such a loose collection of cores can be produced in magnetically subcritical simulations (e.g., see Li & Nakamura 2002; Basu et al. 2009a) influenced by a strong magnetic field. Furthermore, a strong magnetic field will delay the onset of star formation, which may explain the age discrepancy between B1-E and the other nearby clumps in Perseus, IC 348 and NGC 1333.

2. The B1-E clump as a whole is gravitationally bound with an estimated virial parameter of $\alpha \approx 0.9$. Therefore, B1-E is likely to form dense cores and stars. Assuming $T = 14$ K and $n = 5 \times 10^3$ cm^{-3}, we find a Jeans length within the entire B1-E clump of ~ 0.35 pc, accurate within a factor of a few. We measure a median nearest neighbour separation of ~ 0.15 pc for our nine substructures (~ 0.17 pc excluding B1-E6 and B1-E7), for an inclination of 60°. Thus, the substructures have a median minimum separation that is less than the Jeans length by a factor of two. This smaller length scale could indicate that B1-E contracted after the observed substructures formed.

3. Several of the B1-E substructures have masses on order of the Jeans mass (~ 0.9 M$_\odot$), assuming $T = 10$ K and $n = 1 \times 10^5$ cm^{-3}. Nevertheless, most substructures have large virial parameters ($\alpha >> 2$) indicating that they are gravitationally unbound. The large virial parameter suggests that non-thermal motions are significant and that the Jeans mass does not well represent the critical mass scale for these substructures. B1-E2 is the only substructure with a small virial parameter ($1 \lesssim \alpha \lesssim 3$) and, due to its narrow line emission, may be gravitationally bound. Furthermore, NH$_3$ (2,2) and HC$_5$N (9-8) were only detected towards B1-E2. Thus, B1-E2 is an excellent candidate for a core precursor.

4. The B1-E substructures have a substantial centroid velocity dispersion (~ 0.42 km s^{-1}) resulting in an interaction timescale of ~ 1 Myr, assuming an average separation of

~ 0.46 pc. This timescale is well within the lifetime of protostellar cores. Thus, competitive accretion may play a significant role in the evolution of structure in B1-E.

The B1-E region appears to be an excellent candidate for future core formation. Further studies, however, are necessary to explore the dust and dynamics of the bulk gas in B1-E. For example, additional submillimetre continuum data along the Rayleigh-Jeans tail (e.g., with SCUBA-2) will improve SED-fitting and more accurately probe the dust emissivity index, β, size, and mass. To date, our *Herschel* observations of B1-E are the only well detected continuum data for the region. Additionally, our GBT observations are the only high resolution kinematic data for B1-E, and we observed only the nine highest column density substructures seen with *Herschel*. These data illustrate the potential of B1-E to be a core forming region. Future observations of *both* the magnetic field strength and the turbulent velocities are necessary to probe further how B1-E will evolve.

References

Alves, J. F., Lada, C. J., & Lada, E. A. 2001, Nature, 409, 159
André, P., Belloche, A., Motte, F., & Peretto, N. 2007, A&A, 472, 519
André, P., Men'shchikov, A., Bontemps, S., et al. 2010, A&A, 518, L102+
André, P., Men'shchikov, A., Könyves, V., & Arzoumanian, D. 2011, in IAU Symposium, Vol. 270, IAU Symposium, ed. J. Alves, B. G. Elmegreen, J. M. Girart, & V. Trimble, 255–262
André, P. & Saraceno, P. 2005, in ESA Special Publication, Vol. 577, ESA Special Publication, ed. A. Wilson, 179–184
Arzoumanian, D., André, P., Didelon, P., et al. 2011, A&A, 529, L6+
Bachiller, R. & Cernicharo, J. 1986, A&A, 166, 283
Bally, J., Walawender, J., Johnstone, D., Kirk, H., & Goodman, A. 2008, The Perseus Cloud (Handbook of Star Forming Regions, Volume I, ed., by Reipurth, B.), 308–+
Basu, S., Ciolek, G. E., Dapp, W. B., & Wurster, J. 2009a, New A, 14, 483
Basu, S., Ciolek, G. E., & Wurster, J. 2009b, New A, 14, 221
Bergin, E. A. & Tafalla, M. 2007, ARA&A, 45, 339
Bernard, J.-P., Paradis, D., Marshall, D. J., et al. 2010, A&A, 518, L88+
Bonnell, I. A. & Bate, M. R. 2006, MNRAS, 370, 488
Bonnell, I. A., Bate, M. R., Clarke, C. J., & Pringle, J. E. 2001, MNRAS, 323, 785
Bonnor, W. B. 1956, MNRAS, 116, 351
Ceccarelli, C., Caselli, P., Herbst, E., Tielens, A. G. G. M., & Caux, E. 2007, Protostars and Planets V, 47
Curtis, E. I. & Richer, J. S. 2011, MNRAS, 410, 75

Dapp, W. B. & Basu, S. 2009, MNRAS, 395, 1092

Di Francesco, J., Evans, II, N. J., Caselli, P., et al. 2007, in Protostars and Planets V, ed. B. Reipurth, D. Jewitt, & K. Keil, 17–32

Di Francesco, J., Johnstone, D., Kirk, H., MacKenzie, T., & Ledwosinska, E. 2008, ApJS, 175, 277

Di Francesco, J., Myers, P. C., Wilner, D. J., Ohashi, N., & Mardones, D. 2001, ApJ, 562, 770

Dib, S., Kim, J., Vázquez-Semadeni, E., Burkert, A., & Shadmehri, M. 2007, ApJ, 661, 262

Dib, S., Walcher, C. J., Heyer, M., Audit, E., & Loinard, L. 2009, MNRAS, 398, 1201

Doty, S. D. & Leung, C. M. 1994, ApJ, 424, 729

Ebert, R. 1955, Zeitschrift fur Astrophysik, 37, 217

Enoch, M. L., Evans, II, N. J., Sargent, A. I., et al. 2008, ApJ, 684, 1240

Enoch, M. L., Young, K. E., Glenn, J., et al. 2006, ApJ, 638, 293

Evans, II, N. J., Dunham, M. M., Jørgensen, J. K., et al. 2009, ApJS, 181, 321

Friesen, R. K., Di Francesco, J., Shirley, Y. L., & Myers, P. C. 2009, ApJ, 697, 1457

Gong, H. & Ostriker, E. C. 2011, ApJ, 729, 120

Goodman, A. A., Bastien, P., Menard, F., & Myers, P. C. 1990, ApJ, 359, 363

Gregersen, E. M., Evans, II, N. J., Zhou, S., & Choi, M. 1997, ApJ, 484, 256

Griffin, M. J., Abergel, A., Abreu, A., et al. 2010, A&A, 518, L3+

Heiderman, A., Evans, II, N. J., Allen, L. E., Huard, T., & Heyer, M. 2010, ApJ, 723, 1019

Heitsch, F., Naab, T., & Walch, S. 2011, MNRAS, 415, 271

Herbst, W. 2008, Star Formation in IC 348 (Handbook of Star Forming Regions, Volume I, ed., by Reipurth, B.), 372–+

Hirota, T., Bushimata, T., Choi, Y. K., et al. 2008, PASJ, 60, 37

Johnstone, D., Di Francesco, J., & Kirk, H. 2004, ApJ, 611, L45

Jørgensen, J. K., Johnstone, D., Kirk, H., & Myers, P. C. 2007, ApJ, 656, 293

Kirk, H., Johnstone, D., & Di Francesco, J. 2006, ApJ, 646, 1009

Kirk, H., Johnstone, D., & Tafalla, M. 2007, ApJ, 668, 1042

Kirk, J. M., Ward-Thompson, D., & André, P. 2005, MNRAS, 360, 1506

Könyves, V., André, P., Men'shchikov, A., et al. 2010, A&A, 518, L106+

Krumholz, M. R., Cunningham, A. J., Klein, R. I., & McKee, C. F. 2010, ApJ, 713, 1120

Krumholz, M. R., McKee, C. F., & Klein, R. I. 2005, Nature, 438, 332

Kukolich, S. G. 1967, Physical Review, 156, 83

Kunz, M. W. & Mouschovias, T. C. 2009, MNRAS, 399, L94

Lada, C. J., Lombardi, M., & Alves, J. F. 2009, ApJ, 703, 52

Lada, C. J., Lombardi, M., & Alves, J. F. 2010, ApJ, 724, 687

Larson, R. B. 1981, MNRAS, 194, 809

Li, Z.-Y. & Nakamura, F. 2002, ApJ, 578, 256

Li, Z.-Y. & Nakamura, F. 2004, ApJ, 609, L83

Mac Low, M.-M. & Klessen, R. S. 2004, Reviews of Modern Physics, 76, 125

McKee, C. F. 1999, in NATO ASIC Proc. 540: The Origin of Stars and Planetary Systems, ed. C. J. Lada & N. D. Kylafis, 29–+

Mestel, L. & Spitzer, Jr., L. 1956, MNRAS, 116, 503

Miville-Deschênes, M.-A., Martin, P. G., Abergel, A., et al. 2010, A&A, 518, L104+

Mouschovias, T. C. 1976, ApJ, 206, 753

Myers, P. C. 1983, ApJ, 270, 105

Nakamura, F. & Li, Z.-Y. 2008, ApJ, 687, 354

Pineda, J. E., Goodman, A. A., Arce, H. G., et al. 2010, ApJ, 712, L116

Planck Collaboration, Abergel, A., Ade, P. A. R., et al. 2011a, A&A, 536, A24

Planck Collaboration, Abergel, A., Ade, P. A. R., et al. 2011b, A&A, 536, A25

Planck HFI Core Team, Ade, P. A. R., Aghanim, N., et al. 2011, A&A, 536, A6

Poglitsch, A., Waelkens, C., Geis, N., et al. 2010, A&A, 518, L2+

Price, D. J. & Bate, M. R. 2009, MNRAS, 398, 33

Ridge, N. A., Di Francesco, J., Kirk, H., et al. 2006a, AJ, 131, 2921

Ridge, N. A., Schnee, S. L., Goodman, A. A., & Foster, J. B. 2006b, ApJ, 643, 932

Rosolowsky, E. W., Pineda, J. E., Foster, J. B., et al. 2008, ApJS, 175, 509

Rydbeck, O. E. H., Sume, A., Hjalmarson, A., et al. 1977, ApJ, 215, L35

Sault, R. J., Teuben, P. J., & Wright, M. C. H. 1995, in Astronomical Society of the Pacific Conference Series, Vol. 77, Astronomical Data Analysis Software and Systems IV, ed. R. A. Shaw, H. E. Payne, & J. J. E. Hayes, 433–+

Schmalzl, M., Kainulainen, J., Quanz, S. P., et al. 2010, ApJ, 725, 1327

Schnee, S. L., Ridge, N. A., Goodman, A. A., & Li, J. G. 2005, ApJ, 634, 442

Schneider, N., Motte, F., Bontemps, S., et al. 2010, A&A, 518, L83+

Shetty, R., Kauffmann, J., Schnee, S., Goodman, A. A., & Ercolano, B. 2009, ApJ, 696, 2234

Stahler, S. W. & Palla, F. 2005, The Formation of Stars (by Steven W. Stahler, Francesco Palla, pp. 865. ISBN 3-527-40559-3. Wiley-VCH , January 2005.)

Swift, J. J., Welch, W. J., & Di Francesco, J. 2005, ApJ, 620, 823

Walawender, J., Bally, J., Francesco, J. D., Jørgensen, J., & Getman, K. . 2008, NGC 1333: A Nearby Burst of Star Formation (Handbook of Star Forming Regions, Volume I, ed., by Reipurth, B.), 346–+

Ward-Thompson, D., André, P., Crutcher, R., et al. 2007, in Protostars and Planets V, ed. B. Reipurth, D. Jewitt, & K. Keil, 33–46

Ward-Thompson, D., Motte, F., & Andre, P. 1999, MNRAS, 305, 143

Williams, J. P., Blitz, L., & McKee, C. F. 2000, Protostars and Planets IV, 97

Williams, J. P., de Geus, E. J., & Blitz, L. 1994, ApJ, 428, 693

Young, K. E., Lee, J.-E., Evans, II, N. J., Goldsmith, P. F., & Doty, S. D. 2004, ApJ, 614, 252